Supporting Information for

An Experimental- and Simulation-Based Evaluation of the CO_2 Utilization Efficiency of Aqueous-Based Electrochemical CO_2 Reduction Reactors with Ion-Selective Membranes

Meng Lin,[a, b†] Lihao Han,[a,b†] Meenesh R. Singh,[c] Chengxiang Xiang[a, b*]*

[a]Joint Center for Artificial Photosynthesis, and Division of Chemistry and Chemical Engineering, California Institute of Technology, Pasadena, California 91125, United States

[b]Division of Chemistry and Chemical Engineering, California Institute of Technology, Pasadena, CA 91125, USA

[c]Department of Chemical Engineering, University of Illinois at Chicago, Chicago, Illinois 60607

*To whom correspondence should be addressed: cxx@caltech.edu, mrsingh@uic.edu

† Meng Lin and Lihao Han contributed equally to this work.

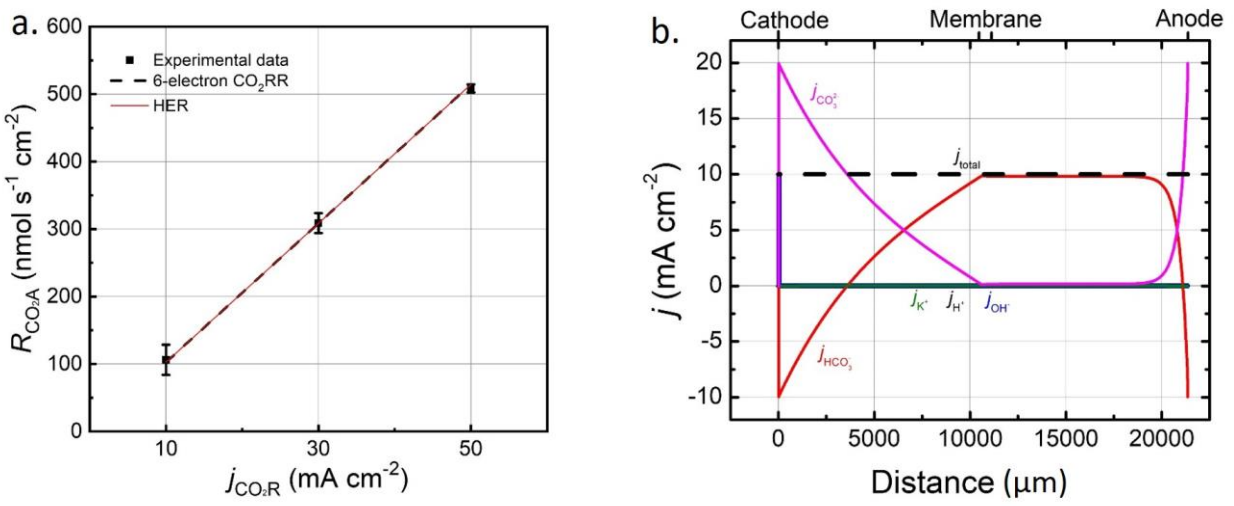

Figure S1. (a) The effect of cathodic reactions (CO_2RR and HER) on the CO_2 loss rate for AEM-based reactor. (b) Partial current density as a function of distance from the cathode surface for an applied current density of 10 mA cm^{-2} with 100% Faradaic efficiency HER.

Figure S1 shows that the CO_2 loss rates are identical for 100% HER and 100% 6-electron CO_2RR due to the dominating partial current carried by HCO_3^-(see figure S1 b).

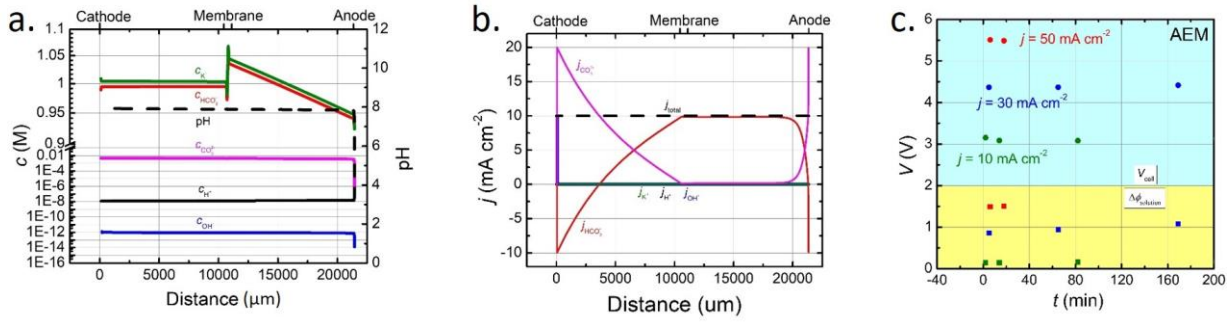

Figure S2. (a) Concentrations of ionic species (solid lines) and pH (dash line) values in solution as a function of distance for applied current density of 10 mA cm^{-2} at the steady-state condition for AEM reactor. (b) Partial current density as a function of distance from the cathode surface for applied current density of 10 mA cm^{-2}. (c) Experimentally measured $\Delta\phi_{\text{solution}}$ (yellow region) and V_{cell} (light blue region) as a function of time for the applied current densities of 10 (in green), 30 (in blue) and 50 mA cm^{-2} (in red).

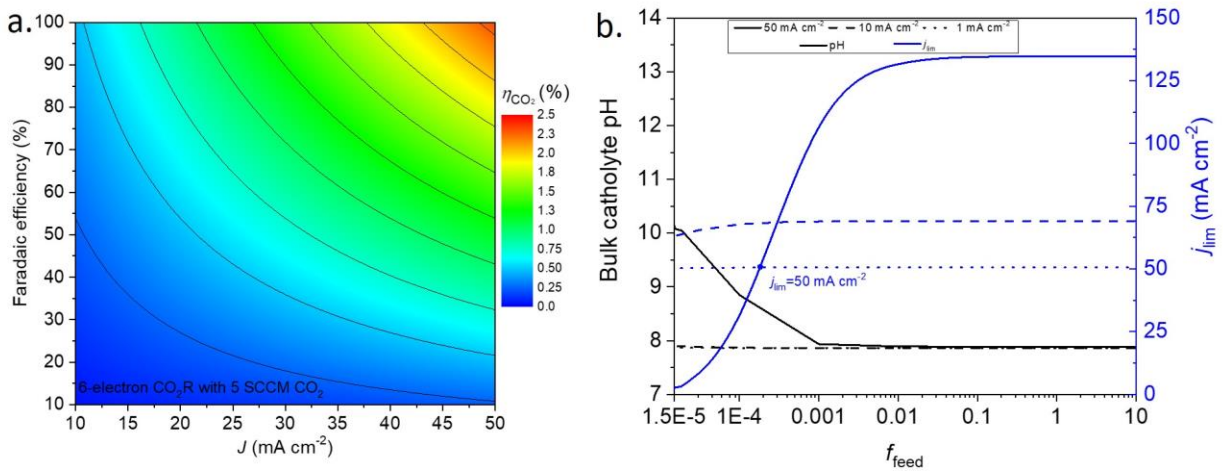

Figure S3. (a) The effect of Faradaic efficiency of the 6-electron CO_2RR and total operation current density on the η_{CO2} with 5 sccm CO_2 feeding rate. (b) Catholyte bulk pH and limiting current density (j_{lim}) for 6-electron CO_2RR as a function of reduced CO_2 feed rate. The black dots indicate the limiting current density of 1, 10, and 50 mA cm^{-2}.

Figure S4 shows the R_{CO2A} and $j_{CO2R,loss,eq}$ as a function operation current for 1 cm and 1mm electrode-membrane space. The CO_2 loss behavior was found to be independent of the electrode-membrane space. The current simulations and previously reported data confirm that there are larger pH gradients and concentration gradients near the electrodes in the dilute electrolyte at operating current densities.[1,2] For the case of lower $KHCO_3$ concentrations, there will be higher K^+ and other anion concentrations near the cathode at any operating current density. The diffusion coefficients of ions in this concentrated layer will be lower as compared to diffusion coefficients of ions in the bulk, whose effect is to reduce the overall operating current density. A similar effect can be seen in Fig. S4, where within an order of magnitude reduction in the diffusion coefficient of $HCO3^-$ anions in 0.1M KHCO3 electrolyte brings the simulated current density closer to the experimental value.

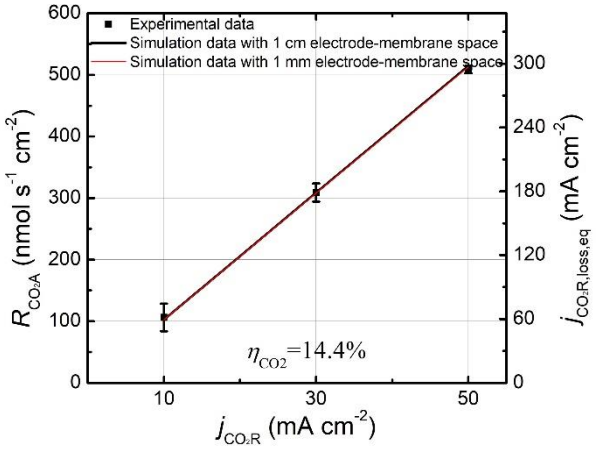

Figure S4. The effect of electrode-membrane space on the CO_2 loss rate for AEM-based reactor.

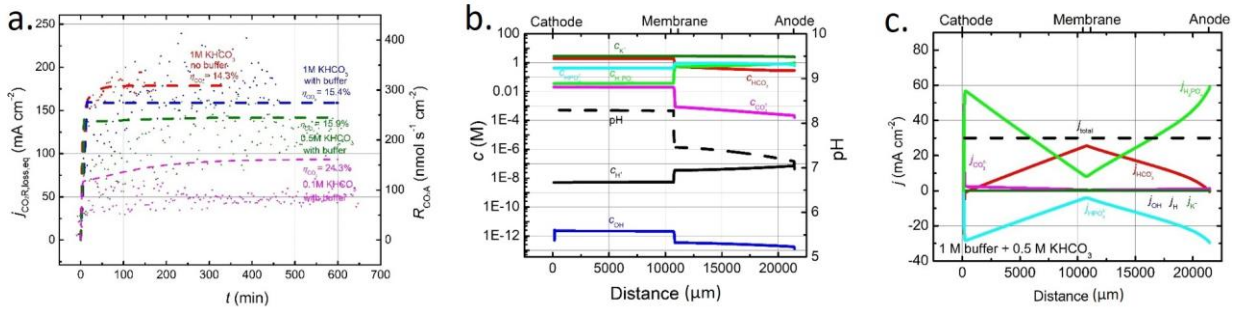

Figure S5. (a) Transient behavior of $j_{CO_2R,loss,eq}$ and η_{CO_2} of AEM cell for the cases with (data in blue, green, and pink are 1 M, 0.5 M, and 0.1 M $KHCO_3$ case, respectively) and without (data in red is 1 M $KHCO_3$ case) buffer solution (1 M phosphate) under a fix operating current density of 30 mA cm^{-2} . Dots are experimental data and lines are simulation data. (b) Species concentration and pH as a function of distance from the cathode surface for the case with 1 M $KHCO_3$ and 1 M phosphate buffer solution under applied current density of 30 mA cm^{-2}. (c) Partial current density as a function of distance from the cathode surface for the case with 0.5 M $KHCO_3$ and 1 M phosphate buffer solution under applied current density of 30 mA cm^{-2} at steady state condition.

The current simulations and previously reported data confirm that there are larger pH gradients and concentration gradients near the electrodes in the dilute electrolyte at operating current densities.[21,26] For the case of lower $KHCO_3$ concentrations, there will be higher K^+ and other anion concentrations near the cathode at any operating current density. The diffusion coefficients of ions in this concentrated layer will be lower as compared to diffusion coefficients of ions in the bulk, whose effect is to reduce the overall operating current density. A similar effect can be seen in Fig. S5, where within an order of magnitude reduction in the diffusion coefficient of HCO_3^- anions in 0.1M $KHCO_3$ electrolyte brings the simulated current density closer to the experimental value.

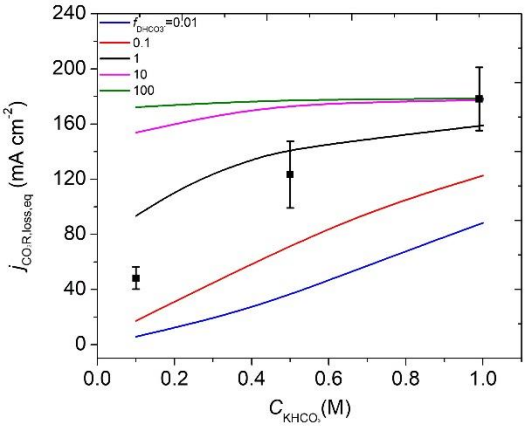

Figure S6. The $j_{CO_2R,loss,eq}$ as a function of $KHCO_3$ concentration for various HCO_3^- diffusion coefficient factors.

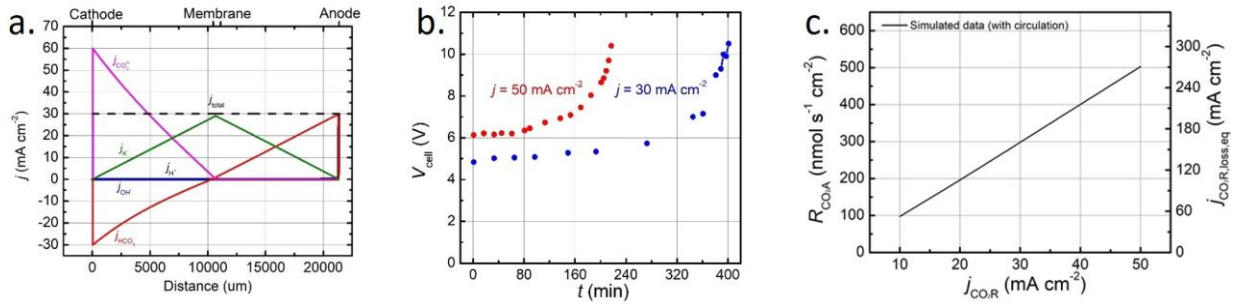

Figure S7. (a) Partial current density as a function of distance from the cathode surface for the CEM reactor with an applied current density of 30 mA cm^{-2} at $\Delta\phi_{solution}$ = 4 V. (b) Measured cell potential (working electrode versus counter electrode) as a function of time for 30 and 50 mA cm^{-2}. (c) The R_{CO_2A} and the $j_{CO_2R,loss,eq}$ as a function of operating current density for the CEM-based reactor with electrolyte re-circulation.

Fig. S7d shows the modeling (dashed lines) and the experimental measurements (dots) of the time-dependent behavior of R_{CO_2A} and the corresponding $j_{CO_2R,loss,eq}$ at two different operating current densities – 30 and 50 mA cm^{-2}. The initial large R_{CO_2A} observed at the anode gas outlet was due to the de-gassing of pre-bubbled CO_2 in the $KHCO_3$ solution in the anode chamber.

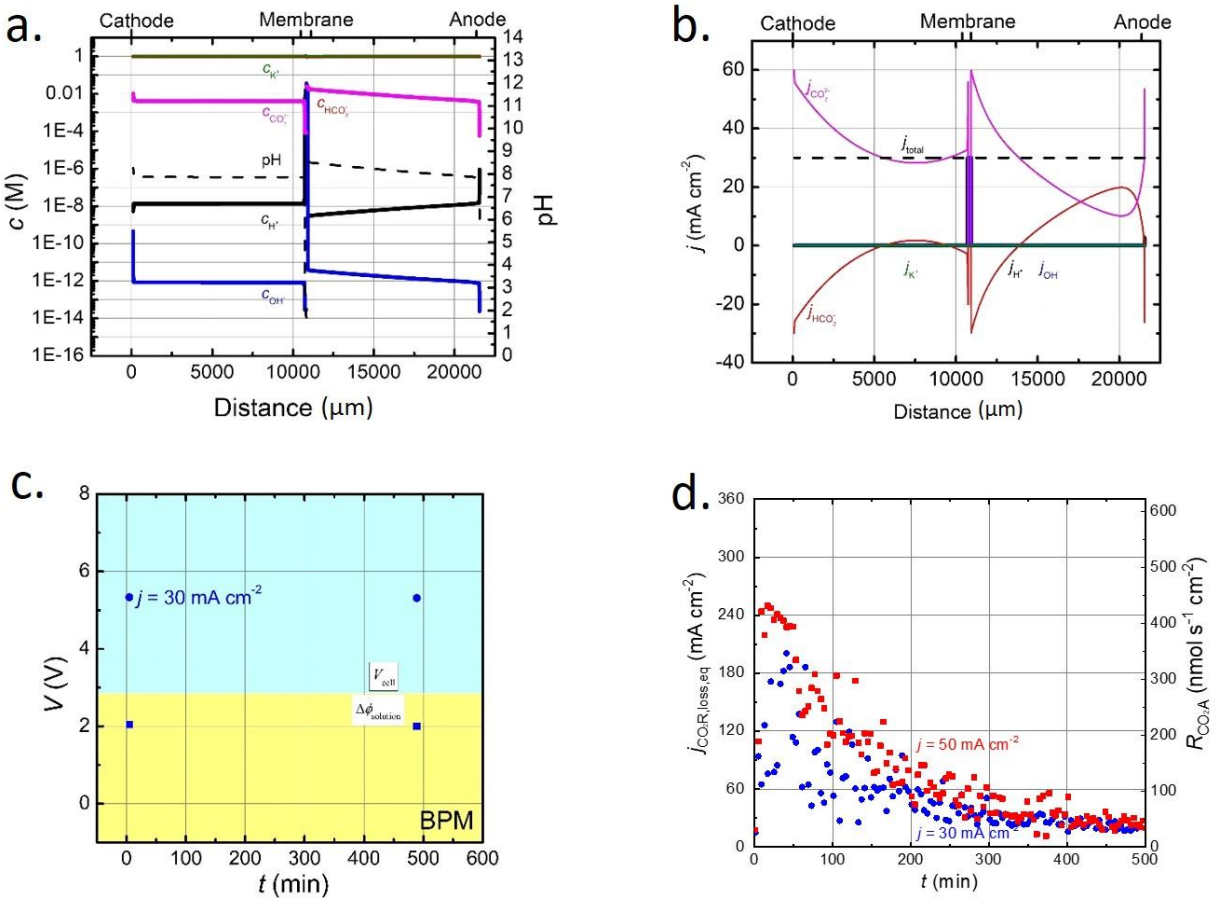

Figure S8. (a) Species concentration and pH and (b) partial current density as a function of distance from the cathode surface for the BPM-based reactor under an applied current density of 30 mA cm^{-2} at steady state condition. (c) Experimentally measured $\Delta\phi_{solution}$ (yellow region) and V_{cell} (light blue region) as a function of time for the applied current densities of 30 mA cm^{-2} (in blue). (d) Transient behavior $j_{CO_2R,loss,eq}$ and η_{CO_2} for different operating current densities (50 mA cm^{-2} in red and 30 mA cm^{-2} in blue).

Computational method

A 1D, isothermal, time-dependent model was developed for three types CO_2R cells considering the species transport (electrolyte and membrane), charge transfer (all components), and surface electrochemical reactions (electrode surfaces). The 1D simulation domains along the *x*-axis are shown in figure 1a, 2a, and 3a for AEM, CEM, and BPM cells, respectively. Boundary layers are included for each solid-liquid interface with a current-density dependent thickness.[3] The thickness of AEM, CEM, and BPM are listed in Table S4.

A time-dependent continuity equation was solved for each species:

$$\frac{\partial c_i}{\partial t} + \nabla N_i = R_i \qquad \text{(S1)}$$

where c_i is the molar concentration, N_i is the molar flux, and R_i is the volumetric rate of species i due to reactions (Eqs. S3-S8). Infinite water disassociation kinetics was assumed at the AEM/CEM interface with the R_i for H^+ and OH^- generation at the interface determined by the current density ($R_i = j/F$). The Nernst-Planck equation is calculated for the molar flux considering migration due to electrical field and diffusion due to concentration gradients:

$$N_i = -D_i \nabla c_i - z_i \frac{D_i}{RT} F c_i \nabla \phi_1 \qquad \text{(S2)}$$

where D_i and z_i are the diffusivity and charge of species, respectively, and ϕ_1 is the electrolyte potential. The D_i for each species used in this study are listed in table 1.[4,5] The species transport in ion-exchange membrane were modeled as electrolyte with reduced diffusion coefficients. The cations diffusion coefficients were reduced by 10 times and anions were reduced by 100 times in CEM. Similarly, the cation and anion diffusion coefficients were reduced by 100 and 10 times,

respectively in AEM. The BPM was modeled as a two-layer structure comprised of AEM and CEM.[1] The chemical reactions included in the electrolyte solution in this study which are contributed to the reaction source term (R_i) are:

$$CO_2+H_2O \overset{k_{1+},k_{1-}}{\longleftrightarrow} H^+ + HCO_3^- \qquad \text{(S3)}$$

$$HCO_3^- \overset{k_{2+},k_{2-}}{\longleftrightarrow} H^+ + CO_3^{2-} \qquad \text{(S4)}$$

$$CO_2+OH^- \overset{k_{3+},k_{3-}}{\longleftrightarrow} H^+ + CO_3^{2-} \qquad \text{(S5)}$$

$$HCO_3^- + OH^- \overset{k_{4+},k_{4-}}{\longleftrightarrow} H_2O + CO_3^{2-} \qquad \text{(S6)}$$

$$H_2O \overset{k_{5+},k_{5-}}{\longleftrightarrow} H^+ + OH^- \qquad \text{(S7)}$$

$$H_2PO_4^{2-} \overset{k_{6+},k_{6-}}{\longleftrightarrow} H^+ + HPO_4^- \qquad \text{(S8)}$$

where k_j and k_{j-} are the forward (left to right) and backward reaction rate constants for reaction j. Reaction rate constants and equilibrium coefficients for Eqs. S3-S8 are listed in table 2.[6] Note that reaction 6 (Eq. S8) is only considered in the buffered AEM case.

The half-cell electrochemical reaction at the anode surface is the water oxidation:

$$H_2O \rightarrow 0.5O_2+2H^+ + 2e^- \qquad \text{(S9)}$$

The cathode electrochemical reactions considered in this study is the reduction of CO_2 into C_2H_4:

$$CO_2+4H_2O+6e^- \rightarrow 0.5C_2H_4+6OH^- \qquad \text{(S10)}$$

We only consider C_2H_4 generation in this study as an exemplary case which can be furthered adapted for other products and we focus more on the CO_2 utilization behavior under varies cell design and operating conditions. Hence, the kinetic overpotential due to electrochemical reactions was not considered as CO_2 transport behavior within the cell will not be affected.

The equilibrium of CO_2 between gas and liquid phase is predicted by Henry's constant (33 mol m^{-3} at 298 K and 1 atm). The CO_2 concentration is constant and uniform over the catholyte (well-mixed electrolyte) since the catholyte is under continuous CO_2 bubbling and circulation. At anolyte, a supersaturation (S) dependent volumetric CO_2 release rate is given by

$$\dot{R}_{CO_2} = \gamma_{CO_2} S^2 \ (S>1) \qquad \text{(S11)}$$

where γ_{CO_2} is the CO_2 loss coefficient (1.25×10^{14} nmol $s^{-1}cm^{-3}$, reported by Wilt and 1.25×10^{7} nmol $s^{-1}cm^{-3}$, adjusted in this study). The physical meaning of CO_2 releasing coefficient (γ_{CO_2}) is the gaseous CO_2 escaping rate (mol s^{-1}) per unit volume (m^{-3}) electrolyte through nucleation of gas bubbles in the electrolyte. Equation 7 of [1] relates the rate of nucleation of gas bubbles to the supersaturation of dissolved CO2 as-

$$R_{CO_2} = N\left[\frac{4\sigma}{3\pi M_w}\right]^{1/2} exp\left[\frac{-16\pi\sigma^3}{3kT(S-1)^2 p_L^2}\right] \qquad \text{(S12)}$$

where N is the moles of CO_2 nucleating at the active sites per unit area, σ is the gas-liquid surface energy which is a function of contact angle with the electrode and the roughness of the electrode, M_w is the molecular weight of CO_2, k is the Boltzmann constant, T is the temperature, S is the supersaturation ratio for CO_2, and p_L is the pressure of CO_2 in the liquid. At higher supersaturation, the

$$R_{CO_2} \approx N\left[\frac{4\sigma}{3\pi M_w}\right]^{1/2}\left[\frac{3kTp_L^2}{16\pi\sigma^3}\right]S^2 \qquad \text{(S13)}$$

The CO_2 releasing coefficient is therefore given as

$$\gamma_{CO_2} = N\left[\frac{4\sigma}{3\pi M_w}\right]^{1/2}\left[\frac{3kTp_L^2}{16\pi\sigma^3}\right] \qquad \text{(S14)}$$

The releasing coefficient depends exponentially on the contact angle and the roughness of the surface where gas bubbles are nucleating. Wilt [25] showed that the rate of nucleation can vary over 7 orders of magnitude with changes in the surface roughness. In the present study, the lower value of CO_2 releasing coefficient is may be due to smoother electrode surface with fewer sites to nucleate CO_2 bubbles.

The partial differential and algebraic equations are solved by via finite element methods and the MUMPS solver in COMSOL5.3a. The polarization loss due to ohmic and diffusion losses in the electrolyte are combined as the solution loss:

$$\Delta\phi_{\text{solution}} = \int \frac{j}{k}\,\mathrm{d}x + \sum_i \int \frac{Fz_iD_i\nabla c_i}{k}\,\mathrm{d}x \qquad \text{(S15)}$$

The first term on the right is the ohmic loss and the second term is the diffusion loss.

Table S1. Diffusion coefficients of each species in aqueous solution.

Species	Diffusion coefficient
H^+	1.9×10^{-5} cm^2 s^{-1}
OH^-	9.3×10^{-5} cm^2 s^{-1}
HCO_3^-	1.2×10^{-5} cm^2 s^{-1}
CO_3^{2-}	0.9×10^{-5} cm^2 s^{-1}
CO_2	1.9×10^{-5} cm^2 s^{-1}
$H_2PO_4^{2-}$	0.88×10^{-5} cm^2 s^{-1}
HPO_4^-	0.44×10^{-5} cm^2 s^{-1}

Table S2. Rate Constants of reactions used in the simulation.

Reactions	Rates
$CO_2+H_2O \overset{k_{1+},k_{1-}}{\longleftrightarrow} H^++HCO_3^-$	$k_{1+}=0.037$ s^{-1} $k_{1-}=7.83\times10^4$ M^{-1} s^{-1}
$HCO_3^- \overset{k_{2+},k_{2-}}{\longleftrightarrow} H^++CO_3^{2-}$	$k_{2+}=2.5$ s^{-1} $k_{2-}=5\times10^{-10}$ M^{-1} s^{-1}
$CO_2+OH^- \overset{k_{3+},k_{3-}}{\longleftrightarrow} H^++CO_3^{2-}$	$k_{3+}=2.23\times10^3$ M^{-1} s^{-1} $k_{3-}=4.85\times10^{-5}$ s^{-1}
$HCO_3^-+OH^- \overset{k_{4+},k_{4-}}{\longleftrightarrow} H_2O+CO_3^{2-}$	$k_{4+}=6\times10^9$ M^{-1} s^{-1} $k_{4-}=1.2$ s^{-1}
$H_2O \overset{k_{5+},k_{5-}}{\longleftrightarrow} H^++OH^-$	$k_{5+}=2.4\times10^{-6}$ M s^{-1} $k_{5-}=2.4\times10^9$ M^{-1} s^{-1}
$H_2PO_4^{2-} \overset{k_{6+},k_{6-}}{\longleftrightarrow} H^++HPO_4^-$	$k_{6+}=1\times10^6$ s^{-1} $k_{6-}=1.622\times10^{13}$ M^{-1} s^{-1}

Experimental method

1. Chemicals and membranes:

The following chemicals without further treatment were used as a solute in the work:

Table S3. Chemicals used in this work

Molecular	Chemical name	Company	CAS #	Purity
$KHCO_3$	Potassium bicarbonate	J.T. Baker	298-14-6	>=99.7%
K_2HPO_4	Potassium hydrogen phosphate	Alfa Aesar	7758-11-4	>=98.0%
KH_2PO_4	Potassium phosphate monobasic	Fisher Scientific	7778-77-0	>=99.0%

The following membranes were used in this work:

Table S4. Membrane details

Membrane type	Company	Brand	Product name	Product code	Thickness
Anion exchange membrane (AEM)	FuelCellStore	FuMA-Tech	Fumasep FAA-3-50	5041646	45 - 55 µm (50 µm used simulation)
Bipolar membrane (BPM)	FuelCellStore	FuMA-Tech	Fumasep FBM	5041614	130 - 160 µm (150 um used in simulation)
Cation exchange membrane (CEM[1])	Ion Power	Nafion	N324	N324-US	~ 100 µm

2. Setups:

Two pieces of 4 cm (H) × 4 cm (W) × 1 cm (D) plastic chambers were stacked together. Each piece has 1 cm × 1 cm window on both sides. The surface areas of the electrodes and membranes were all 1cm x 1cm. The anolyte and catholyte chamber cross-sectional areas are both 4 cm x 4 cm, with a thickness of 1 cm, and the anolyte and catholyte were filled up to ~90% of the chamber volume of 16 mL in each chamber). There are a few important details of this design: 1) ~10% headspace of the electrolyte chamber is required for delivering the N_2 carrier gas in and out without contaminating the flow meter and the gas chromatography in the downstream. That's why we filled in ~14.5 mL electrolyte in the 4 cm x 4 cm x 1 cm chamber, 2) the whole electrode area has to be immersed completely in the electrolyte, so two Ni electrodes with a smaller area of 1 cm x 1 cm were used, and 3) all of our electrolyte was CO_2 pre-bubbled, and the saturated concentration of CO2 would not make our experiments CO_2 limited. A piece of membrane (AEM, BPM or CEM) was inserted between the two chambers, and two pieces of nickel (Ni) were sealed on the outer side of both chambers, acting as cathode and anode, respectively. Constant current (10, 30 or 50 mA) was applied between the two electrodes by an SP-200 Potentiostat (Bio-Logic Scientific Instruments).

The cathode chamber was filled with CO_2-pre saturated 1M $KHCO_3$ aqueous electrolyte, which was continuously recycling with "fresher" 1M $KHCO_3$ electrolyte being bubbled by 25 sccm CO_2 (Airgas USA LLC, UHP Grade 3.0). The anode chamber was filled with the same CO_2-pre saturated 1M $KHCO_3$ aqueous electrolyte, and 50 sccm N_2 (Airgas USA LLC, UHP Grade 3.0) was flowing from the small headspace and transporting the sample into the gas chromatography (GC, SRI Instruments 8610C) for analysis. Two conventional Ag/AgCl electrodes (in 1M KCl, CH instruments Inc., CHI111_L) were placed in the center of the cathode and anode chambers, respectively. The average voltage between these two electrodes was measured intermittently.

An online GC was customized for the gas product analysis. In a traditional dual-detector GC, the injected sample gas flows through a thermal conductivity detector (TCD) and then a flame ionization detector (FID) in a tandem configuration. The signals from the same type of gas can be displayed in both chromatography channels simultaneously. An obvious disadvantage of this configuration is the long analyzing time of one measurement. In order to increase the time resolution in the online system, we modified the in-series configuration into in-parallel configuration: O_2 was detected by the TCD after flowing through a 6-inch HAYESEP-D column and a 6-inch MS 5A column, and CO_2 was detected by the FID simultaneously after flowing through an 18-inch HAYESEP-D column in parallel and a methanizer converting CO_2 into detectable CH_4.

Ar (Ultra High Purity 5.0 Grade, Airgas West Inc.) was used as the carrier gas in the online GC system, and its inlet pressure was controlled at an optimized value of 20 PSI. TCD low mode and FID medium mode were chosen to ensure an optimal characterization setting: enough sensitivity and simultaneously no peak saturation. The GC was continuously running during the whole experiment and collecting the area for each species every 4 min. Fig. S9 shows the peak area of O_2 and CO_2 with known concentrations from our calibration gas cylinders (concentration error within relative ±2.0% certificated by Airgas West Inc.) under these settings. For an accuracy of the analysis, all the measured GC areas should be within the calibrated range. The high (close to 1) coefficient of determination ensures the accuracy in quantitatively determining the concentration of each species. We want to point out that the FID responses became less linear as the CO_2 concentration increased. When many ions were created at once, they drifted over to the positively charged collector electrode in the GC. They form a cloud of negative charges which

repels more negative ions, thus, some of the ions could never reach the positive electrode. Piecewise functions were used for CO_2 calibration to compensate for this "space charge effect".

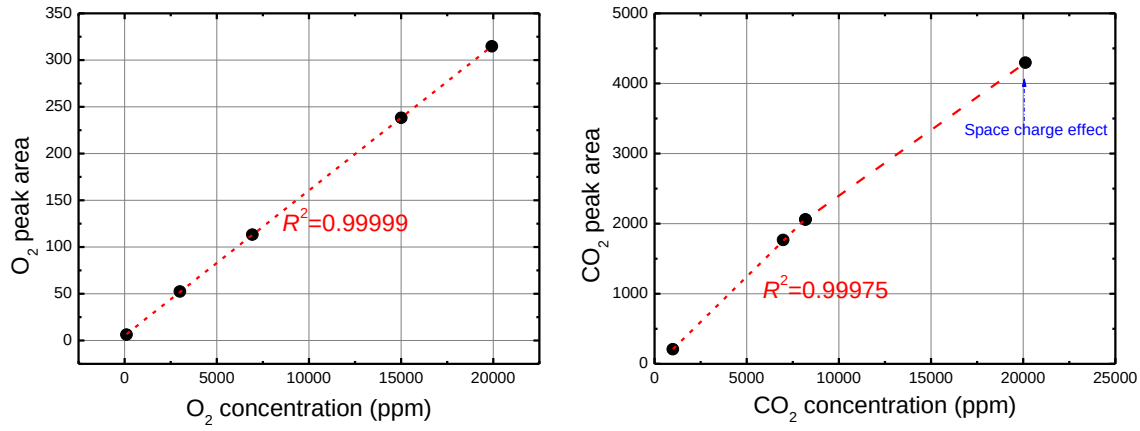

Figure S9. Integrated peak areas from customized GC flowing configuration as a function of the concentration of calibration gas (O_2 and CO_2) with known concentration.

3. Electrochemical reactions:

In most experiments, CO_2-pre-saturated 1 M $KHCO_3$ (without any buffer solution) was used as the electrolyte to test the CO_2 releasing rate under different constant current (10, 30 and 50 mA) and membrane conditions (AEM/BPM/CEM). When current was applied between the two electrodes, H_2 gases was evolving from the surface of the cathode Ni plate and transported away by the recycling electrolyte. These H_2 bubbles were released into the extractor arm from a recycling beaker connected with the cathode chamber, and meanwhile, 25 sccm CO_2 was continuously bubbling through the 1 M $KHCO_3$ electrolyte in the beaker, making sure sufficient bicarbonate species were available in the cathode chamber. Simultaneously, O_2 gases were evolving from the surface of the anode Ni plate, and CO_2 bubbles were released due to the dynamic equilibrium of the increasing concentration of bicarbonate species on the anode chamber. The mixture of O_2 and

CO_2 bubbles was transported into GC by a 50 sccm N_2 carrier gas flow or concentration determination. The pH values of each solution before and after the electrochemical reactions were measured using a calibrated pH meter (Denver Instrument pH/mV Meter, UB-10, accuracy: 0.005 pH).

In the AEM experiment, different concentrations of 0.1, 0.5 and 1 M $KHCO_3$ solutions were used as the electrolyte for comparison. In order to keep the anion concentrations at 1 M in each experiment, various combinations of K_2HPO_4 and KH_2PO_4 buffer solution were mixed into the $KHCO_3$ electrolyte. The species concentrations of these buffer solutions were calculated according to Henderson-Hasselbalch Equation, and then double-confirmed by the pH meter, making sure the pH values of the $KHCO_3$ solutions were kept constant before and after adding these buffer solutions.

Table S5 Solution compositions (with and without buffer solution) and measured pH values

Experiment	$KHCO_3$	K_2HPO_4	KH_2PO_4	pH value
I (no buffer)	1 M	0 M	0 M	7.85
II (with buffer)	1 M	0.81293 M	0.18707 M	7.85
III (with buffer)	0.5 M	0.68567 M	0.31433 M	7.55
IV (with buffer)	0.1 M	0.30443 M	0.69557 M	6.85

REFERENCES

(1) Singh, M. R.; Clark, E. L.; Bell, A. T. Effects of Electrolyte, Catalyst, and Membrane Composition and Operating Conditions on the Performance of Solar-Driven Electrochemical Reduction of Carbon Dioxide. *Phys. Chem. Chem. Phys.* **2015**, *17* (29), 18924–18936.

(2) Singh, M. R.; Bell, A. T. Design of an Artificial Photosynthetic System for Production of Alcohols in High Concentration from CO2. *Energy Environ. Sci.* **2016**, *9* (1), 193–199.

(3) Sequeira, C. A. C.; Santos, D. M. F.; Šljukić, B.; Amaral, L. Physics of Electrolytic Gas Evolution. *Brazilian Journal of Physics*. 2013, pp 199–208.

(4) P, D. CRC Handbook of Chemistry and Physics. *J. Mol. Struct.* **1992**, *268* (1–3), 320.

(5) Johnson, K. S. Carbon Dioxide Hydration and Dehydration Kinetics in Seawater. *Limnol. Oceanogr.* **1982**, *27* (5), 849–855.

(6) Schulz, K. G.; Riebesell, U.; Rost, B.; Thoms, S.; Zeebe, R. E. Determination of the Rate Constants for the Carbon Dioxide to Bicarbonate Inter-Conversion in PH-Buffered Seawater Systems. *Mar. Chem.* **2006**, *100* (1–2), 53–65.